

# Automated microscope-independent fluorescence-guided micropipette

CHRISTOPHER MIRANDA,<sup>1</sup>  MADELEINE R. HOWELL,<sup>1</sup> JOEL F. LUSK,<sup>1</sup> ETHAN MARSHALL,<sup>1</sup> JARRETT ESHIMA,<sup>1</sup> TRENT ANDERSON,<sup>2</sup> AND BARBARA S. SMITH<sup>1,\*</sup> 

<sup>1</sup>Arizona State University, School of Biological and Health Systems Engineering, Tempe, AZ 85210, USA

<sup>2</sup>University of Arizona, College of Medicine – Phoenix, Phoenix, AZ 85004, USA

\*BarbaraSmith@asu.edu

**Abstract:** Glass micropipette electrodes are commonly used to provide high resolution recordings of neurons. Although it is the gold standard for single cell recordings, it is highly dependent on the skill of the electrophysiologist. Here, we demonstrate a method of guiding micropipette electrodes to neurons by collecting fluorescence at the aperture, using an intra-electrode tapered optical fiber. The use of a tapered fiber for excitation and collection of fluorescence at the micropipette tip couples the feedback mechanism directly to the distance between the target and electrode. In this study, intra-electrode tapered optical fibers provide a targeted robotic approach to labeled neurons that is independent of microscopy.

© 2021 Optical Society of America under the terms of the [OSA Open Access Publishing Agreement](#)

## 1. Introduction

Patch-clamp electrophysiology has been necessary for understanding both inter and intracellular processes of neurons through high resolution electrical recordings [1,2]. This powerful technique has a major barrier to entry due to the training required, low throughput, and dependence on the skill of the electrophysiologist. Recent attempts have been made to circumvent these challenges with the advent of automated micropipette-based patch-clamp systems capable of neuronal targeting, recording, and more recently, micropipette reloading [3–6]. However, these systems remain limited in their ability to target specific neuronal subtypes within the intact brain, where regions of interest are located beyond the imaging depth of current optical microscopy approaches.

The main distinction between different automated patch-clamp systems are the feedback mechanisms used for neuronal targeting, which include blind and image-guided systems. Blind systems utilize resistance measurements, caused by physically blocking current flow through the aperture of the micropipette tip to determine proper placement on the neuron [3,7–10]. Though this technique has proven useful for providing feedback regarding the distance between the micropipette tip and the neuron, it is mainly limited by its inability to target specific neuronal subtypes. To achieve real-time subtype-specific targeting, image-guided systems often leverage the use of fluorescent labels and dyes [5,6,11–13].

These systems utilize high-powered optical imaging techniques, including confocal and two-photon (2P) microscopy, to iteratively locate the neuron and micropipette tip. This approach enables both cellular subtype targeting within heterogeneous environments and the correlation of electrical characteristics to neuronal morphology. Existing *in-vivo* image-guided systems can track cells using fluorescence, but are usually limited to superficial brain regions, such as the uppermost cortical layers where the neurons and the micropipette tip can be reliably resolved [14]. Other non-automated imaging techniques have also been explored, such as: oblique epi-illumination [15], shadowpatching [16], and targeting of fluorescently labeled neurons utilizing fluorescent pipettes [17]. An automated system whose feedback directly reports the

distance between the neuron and micropipette tip (i.e., blind systems), while also allowing for the minimally invasive local detection of fluorescently labeled neurons (i.e., image-guided systems), will offer an improved approach. Such a system would require fluorescence excitation and emission collection at the micropipette tip, enabling a technology that is independent of a microscope.

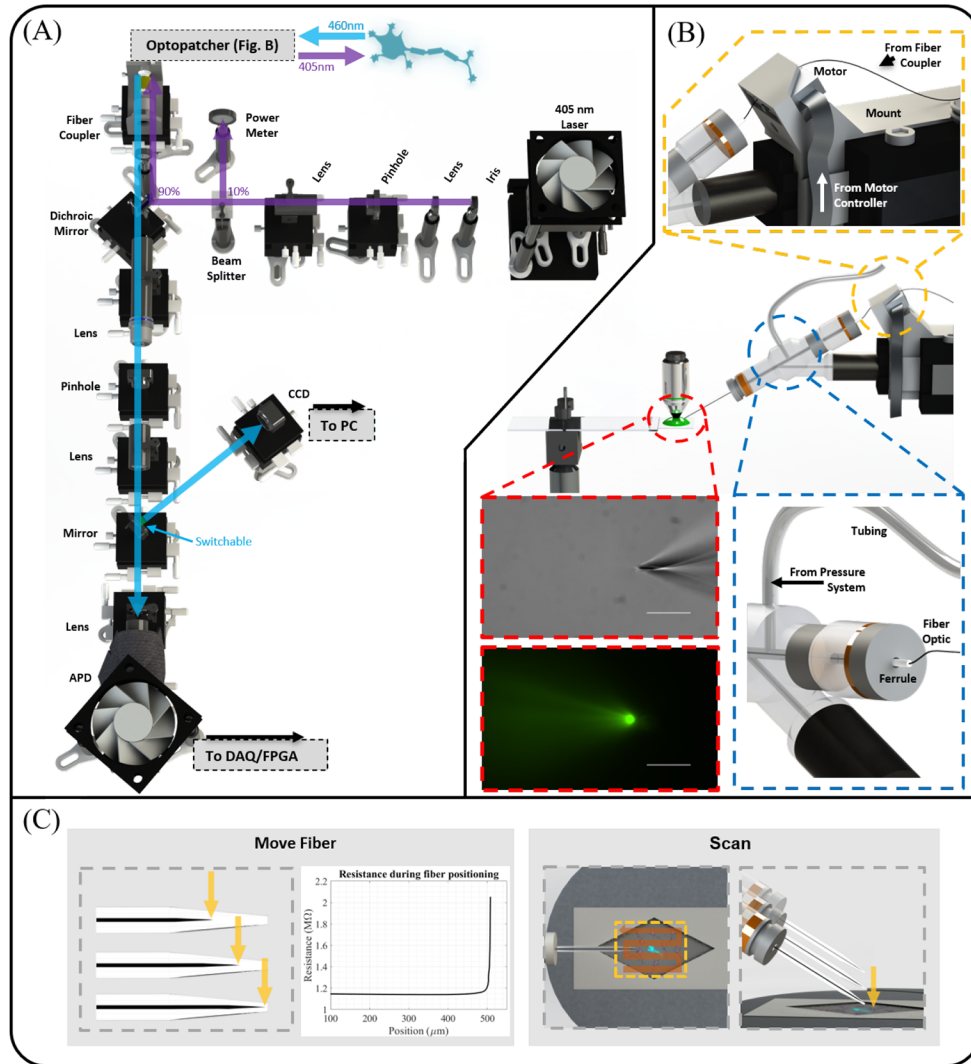


**Fig. 1.** (a) System architecture. Excitation light from 405 nm laser is spatially filtered and sampled using a beam splitter. It is then coupled to the optical fiber. Fluorescence light follows the optical detection path where it is spatially filtered and focused onto a detector. (b) The optical fiber is attached to a linear actuator (yellow box) and enters the electrode holder through a ferrule (blue box). To visualize the beam profile, light exiting the tapered optical fiber is imaged in fluorescein under a FITC filter (red box). 50  $\mu$ m scale bar. (c) Resistance through the micropipette is monitored while the linear actuator moves the tapered optical fiber towards the micropipette tip (left). During automated approach, the micropipette is raster scanned in a 2D plane and descends after each scan (right).

Optical waveguides have been employed to circumvent limitations of imaging depth in several areas of neuroscience. Insertion of waveguides deep into tissue has enabled controlled light delivery, which has been leveraged for a variety of applications including imaging, optogenetics, and photometry [18–21]. Optical detection and manipulation through waveguides combined with direct electrophysiological voltage measurements has been successfully achieved in several ways. In some iterations, the optical and electrophysiological measurements are concentric but not proximal [22–24], while in another they are proximal without being concentric [25,26]. Such disparities can lead to issues with detection sensitivity and spatial resolution. Our recently developed photoacoustic micropipettes (PMP) aim to address these limitations, enabling both concentric and proximal measurements by implementing optical and electrophysiological alignment [27].

In this study, gold-coated tapered optical fibers aligned concentrically and proximally to the micropipette tip were utilized for automated neuronal approach. This was achieved using an Optopatcher [22] retrofitted to allow a micro linear actuator to properly position the tapered optical fiber within the micropipette electrode. The single fiber was coupled to an excitation source and optical detector as shown in Fig. 1(a). The detected fluorescence increased as the tip approached the target due to more efficient excitation and emission. This change in the excitation and emission, resulting from the proximity between the micropipette tip and target, was utilized as feedback for the automated neuronal approach. These experiments were confirmed using traditional epifluorescence microscopy, however, imaging was not utilized as feedback in the algorithm. This technology provides a targeted robotic approach to labeled neurons that is independent of microscopy since the excitation and emission are locally delivered and captured at the electrode aperture.

## 2. Materials and methods

### 2.1. System architecture using intra-electrode tapered optical fiber

The optical architecture is shown in Fig. 1(a). An ultra compact diode laser (IBEAM-SMART-405-S-HP; Toptica Photonics) operated at a 405 nm wavelength and 1-5 mW was used as the excitation source to generate fluorescence. The light source was spatially filtered using two lenses with a 50 mm focal length (ACN127-050-A and LA1131, Thorlabs) and a 50  $\mu\text{m}$  pinhole (P50C, Thorlabs). To sample the power of the excitation beam over time, a beam splitter (BS037, Thorlabs) redirected 10% of the light towards a power meter (S120VC, Thorlabs). Light transmitted through the beam splitter enters an optical enclosure through an excitation filter (ET405/10x, Chroma). It was then redirected by a dichroic mirror (AT440DC, Chroma) to a fiber coupling system (F-91-C1-T, Newport), where the light was focused onto a tapered optical fiber (Nanonics) with a 1.5  $\mu\text{m}$  diameter tip, 0.22 NA, and 125  $\mu\text{m}$  core diameter utilizing a 10x objective (LMH-10x-532, Thorlabs). The tapered fiber passes through a light weight linear micro actuator (XLA-1-20-1250-T, Xeryon) and into an Optopatcher (A-M Systems) fitted with 270  $\mu\text{m}$  inner diameter ferrule (CFLC270-10, Thorlabs). The tapered fiber was placed into a micropipette made from a borosilicate capillary tube with an outer diameter of 1.5 mm and an inner diameter of 1.1 mm. Micropipettes were pulled using a P-87 micropipette puller (Sutter Instruments) to have a 1-1.3 M $\Omega$  resistance. Excitation light, having exited the tapered optical fiber, traveled through the micropipette tip onto the sample or into 30  $\mu\text{M}$  of fluorescein (Fluorescein sodium salt, S46970, Sigma-Aldrich.) in DI water.

Emission light collected by the tapered fiber in the micropipette tip then traveled back into the optical enclosure where it was collimated by the fiber coupling system and passes through the dichroic mirror. The light was then focused with a 40x objective (89403-600, VWR), spatially filtered using a 25  $\mu\text{m}$  pinhole (P25C, Thorlabs), and collimated by a lens with a 50 mm focal length (LA1131, Thorlabs). The light then passed through two emission filters (ET480/40m, Chroma; D460/50m, Chroma). A removable mirror (PF10-03-G01, Thorlabs) can be used

to redirect the beam in the optical enclosure onto a CCD camera (DCC1645C, Thorlabs) for system alignment, or use as a spectrometer (CCS200, Thorlabs). When removed, the emitted light continued through a plano-convex lens (LA1131, Thorlabs) and was focused onto an avalanche photodiode (APD, SPCM-AQR, PerkinElmer). Data acquisition was performed with a multipurpose reconfigurable oscilloscope (NI PXIe-5170R, National Instruments Corporation).

### *2.2. Concentric and proximal alignment of tapered optical fiber within micropipette tip*

Custom LabVIEW software was used to operate the system to achieve fluorescence guided automated neuronal approach. This robotic navigation was performed as a two-part system, including: i) tapered optical fiber positioning and ii) automated navigation of the micropipette [Fig. 1(c)]. In order to assemble the probe, a micromanipulator (Patchstar, Scientifica) was used to carefully navigate the tapered optical fiber into the hollow core of an electrode. The micropipette was then manually fastened into the electrode holder. Resistance changes caused by the integrated optical fiber enable accurate positioning of the fiber tip at the electrode aperture. This was accomplished by submerging the micropipette tip inside a bath under application of low positive pressure (2-8 kPa) to avoid clogging. A voltage pulse was introduced into the micropipette and the resulting current was measured by a patch clamp amplifier (Model 2400, A-M Systems), thus providing a resistance measurement. The algorithm sends ASCII commands to a linear micro-actuator (XLA-1-20-1250-T, Xeryon) to move the tapered fiber over a range of 5 mm in 1.5  $\mu\text{m}$  steps for optimal placement, as shown in Fig. 1(b). When the micropipette resistance increases by roughly 1 M $\Omega$  due to the optical fiber, the algorithm stops moving the micro-actuator. This increase in resistance corresponds to accurate positioning of the tapered fiber for the micropipette architecture used. After each use, the micropipettes can be easily removed and replaced as described above.

### *2.3. Automated fluorescence guided neuronal approach*

To monitor the automated approach to the fluorescent target (Fig. 1(c)), these experiments were performed within the field of view of a DIC microscope (Eclipse FN1, Nikon). The micropipette tip was placed over the sample and the laser was turned on and left idle for 10 seconds, allowing the laser power and APD detection efficiency to stabilize. Laser intensity was kept constant through the entirety of the scan. During experiments, the micropipette travels at a speed of  $\sim 330 \mu\text{m/s}$ . Commands were sent to a micromanipulator (Patchstar, Scientifica) to scan a large region of interest (ROI) in 3  $\mu\text{m}$  steps across the x-y plane, covering a 30 x 33  $\mu\text{m}$  area. A photon count was performed at each step for 60 ms. Following each complete ROI scan there are two possible outcomes based on signal detection. Details of signal criteria are included in 'image processing-based object counting' below. If no signal was identified, the large ROI was centered around the x-y coordinate that corresponded to the peak photon count and the system descends 2  $\mu\text{m}$  along the z-axis, where it performs another scan. This process continues until signal detection occurs. If signal was identified, the system switches to scanning a small ROI centered around the detected signal. This small ROI was scanned in 2  $\mu\text{m}$  steps across the x-y plane, covering an 8 x 6  $\mu\text{m}$  area. Micropipette resistance was measured at each step. After the initial small ROI scan, the micropipette descends 0.5  $\mu\text{m}$  along the z-axis, where it performs another scan. This process continues until resistance increases by 0.1 M $\Omega$ , indicating physical contact between the micropipette tip and the target cell. Once the resistance stop condition was met, the laser was turned off.

### *2.4. Image processing-based object counting*

In order to reliably switch scanning from a large ROI to a small ROI, one of two criteria must be met: i) photon count thresholding and ii) object counting. For the first criteria, the system assumes signal detection if the maximum photon count per scan increases by a user-defined

value. The second criteria implements simple image processing techniques. Photon count rates are represented as an 8-bit image where the pixel location corresponds to each spatial coordinate. To generate a binary image of bright and dark pixels, a threshold was set at 75% between the maximum and minimum photon count rates. A flat linear structuring element, with an angle parallel to the micropipette in the x-y plane, was used to perform image dilation and subsequent image erosion. The resulting image was used to assess the presence of a signal through object counting. Neighboring bright pixels, either vertically, horizontally, or diagonally adjacent, are counted as a single object. If the object count was  $\leq 4$  the system assumes signal detection, thus triggering the switch to the small ROI. The threshold values were experimentally determined to provide accurate signal detection.

### 2.5. Cell culture preparation

The B35 cell line (rat neuroblastoma) was obtained from ATCC (CRL-2754, American Type Culture Collection). B35 cells were cultured in Dulbecco's Modified Eagle Medium (DMEM) supplemented with 10% fetal bovine serum (FBS), 100 U/mL penicillin, and 100  $\mu\text{g/mL}$  streptomycin and were maintained at 37 C in a humidified 5% CO<sub>2</sub> incubator. For electrophysiology experiments, cells were seeded on glass coverslips in a 24 well plate at a density of  $0.071 \times 10^6$  and used within 72 hours. All cells used were at or below passage 5 in this study. Cells were stained with Hoechst 33342 (R37605, ThermoFisher Scientific) by incubating for ~30 minutes. For the neuronal approach experiments, cells were submerged in artificial cerebrospinal fluid (aCSF) with the following components and concentrations: 135 mM NaCl, 2.5 mM KCl, 10 mM HEPES, 2 mM CaCl<sub>2</sub> and 1 mM MgCl<sub>2</sub>. The intracellular pipette solution consisted of (in mM): 135 K gluconate, 4 KCl, 2 NaCl, 10 HEPES, 4 EGTA, and 0.3 Na Tris.

## 3. Results

### 3.1. Optical resolution of intra-electrode tapered optical fiber

Figures 1(a) and (b) show the experimental setup for observing the beam profile. The beam shape of the light exiting the intra-electrode tapered optical fiber was imaged in ~30  $\mu\text{M}$  of fluorescein in DI water. Utilizing a FITC filter and an upright microscope, the emitted fluorescence from the 405 nm beam was captured. Concentric and proximal alignment of the tapered optical fiber and electrode tip was achieved using an optimized micropipette architecture. A starting micropipette resistance between 1.0 - 1.3 M $\Omega$  [Fig. 1(c)] facilitated proper placement of the intra-electrode tapered optical fiber. Once positioned, the distance between the fiber tip and electrode aperture was 1-4  $\mu\text{m}$ .

Modified versions of the raster scans described in Sec. 2.3 were utilized to better understand the resolution of the system. Raster scans with 1 micron-sized steps were performed directly above fluorescent samples of known size. Shown in Fig. 2(a) is a microscope image of a single fluorescent bead (FMB-1.3 1-5 $\mu\text{m}$ , Cospheric), illuminated by excitation light exiting the tapered optical fiber. The raster scan was repeated while dropping 1  $\mu\text{m}$  between each scan until the micropipette tip physically touched the fluorescent bead. The photon count acquired at each location along the scan was converted into an 8-bit pixel value as shown in the reconstruction in Fig. 2(b). The line plots correspond to the row and column of the reconstruction that contains the peak photon count. For simplicity, the z-axis begins at zero corresponding to the minimum signal. Full width half maximum (FWHM) measurements of the normalized data from the microscope and micropipette are shown in Fig. 2(c). Using Matlab software to perform a Gaussian fit, the measured transverse FWHM is ~2.1  $\mu\text{m}$  for the microscope and ~2.9  $\mu\text{m}$  for the intra-electrode tapered optical fiber.

Further experiments were performed on cultured B35 neuroblastoma cells to test the resolution and sensitivity of the system. Shown in Fig. 3(a) is an overlaid image of brightfield (DIC

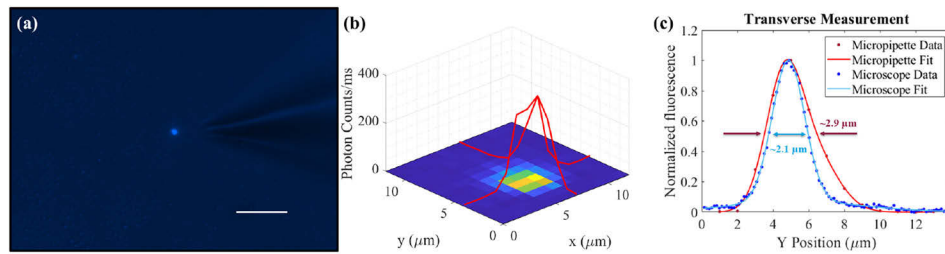


**Fig. 2.** (a) Fluorescent bead with a  $2\ \mu\text{m}$  diameter illuminated by the fluorescence guided electrophysiology system. Scale bar represents  $25\ \mu\text{m}$ . (b) Reconstruction of bead using internal illumination. (c) Full width half maximum measurement of (a) and (b) using a Gaussian fit of microscope data (blue trace) and micropipette data (red trace).

Microscope) and fluorescence. Raster scans were performed with 1 micron-sized steps above the sample, collecting fluorescence from each position. The photon count acquired at each location along the large ROI scan is converted into an 8-bit pixel value as shown in the reconstruction in Fig. 3(b). The line plots correspond to the row and column of the reconstruction that contains the peak photon count. For simplicity, the z-axis begins at zero corresponding to the minimum signal. The FWHM of the cell was measured using both the microscope camera and the fluorescence guided system, as shown in Fig. 3(c). Using MATLAB software to perform a Gaussian fit, the measured transverse FWHM is  $\sim 5.3\ \mu\text{m}$  for the microscope and  $\sim 7.7\ \mu\text{m}$  for the intra-electrode tapered optical fiber.

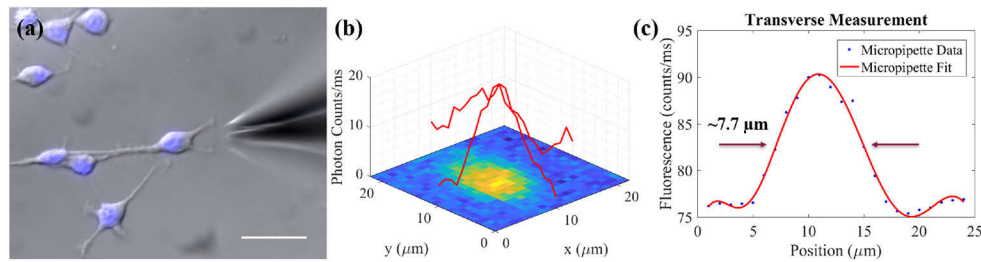


**Fig. 3.** (a) Overlaid image of brightfield and fluorescence (DAPI Filter Set). Scale bar is  $25\ \mu\text{m}$ . (b) Reconstruction of center neuron in (a). Z axis represents photon counts above the minimum count. (c) Transverse measurement of (b).

### 3.2. Automated navigational approach

Figure 4 demonstrates automated approach towards fluorescent beads. For clarity, only the position within each ROI scan corresponding to the peak fluorescent signal were plotted to produce the trajectories. Aggregated fluorescent beads with a cumulative diameter of  $\sim 10\ \mu\text{m}$  were utilized for this experiment. Since the beads cannot provide a reliable increase in resistance, a safe distance between the micropipette tip and the sample was maintained during automated navigation by using a photon count stop threshold. A photon count stop threshold of 700 photon counts/ms was experimentally determined by manually placing the tip near the fluorescent beads. From this position, the micropipette tip was moved  $+50\ \mu\text{m}$  in the x, y, and z directions. The approach algorithm was run, until a stop threshold was reached (red trajectory). From this stop position, the micropipette tip was moved  $+50\ \mu\text{m}$  in the x and z directions, however, was then shifted  $-50\ \mu\text{m}$  in the y direction. The approach algorithm was again run from this starting position (green trajectory), until the stop threshold was reached. Lastly, the micropipette tip was

moved  $+50\ \mu\text{m}$  in the  $x$  and  $z$  directions, however, it was not moved in the  $y$  direction. Following this, the approach algorithm was run again (black trajectory). The starting points differed up to  $\sim 100\ \mu\text{m}$ , yet the algorithm placed the micropipette tips within 3 microns of each other, as shown in Fig. 4(b). As the micropipette tip approached the fluorescent beads the overall collected signal increases non-linearly, as shown in Fig. 4(c).

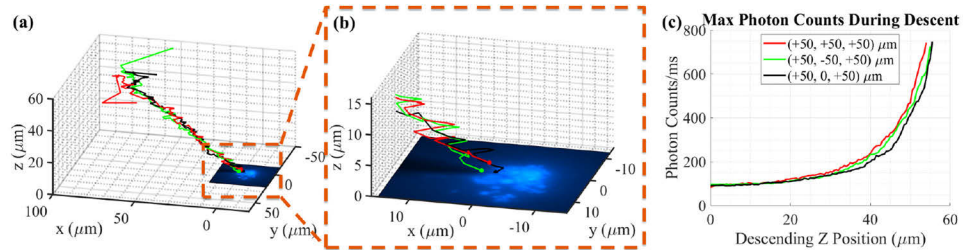


**Fig. 4.** (a) Peak count positions during ROI scans to a  $\sim 10\ \mu\text{m}$  aggregation of fluorescent beads. (b) End points for the three trajectories. (c) Fluorescence as a function of descent.

Shown in Fig. 5 are the results from automated neuronal approach towards fluorescently labeled cells. In contrast to the fluorescent beads an increase in resistance was utilized as the stop condition. The micropipette tip was coarsely aligned above a B35 neuroblastoma cell within the

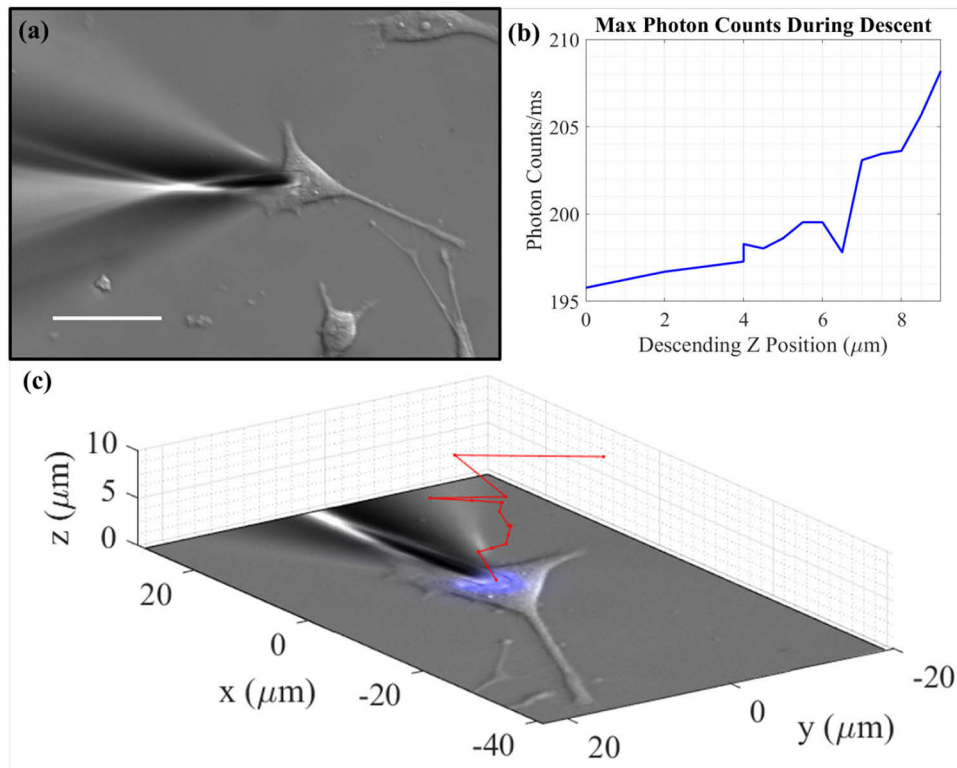


**Fig. 5.** (a) Final position after automated approach of stained B35 neuroblastoma cell. Scale bar represents  $25\ \mu\text{m}$ . (b) Max photon count/ms per scan during descent. (c) Trajectory of micropipette tip plotted over composite image of brightfield and fluorescence (DAPI Filter Set).

field of view of the DIC microscope and the algorithm was run. The image processing-based object counting approach was used to determine the presence of signal because of the relatively small increase in maximum photon counts. The detection of a signal triggered a switch from large ROI to small ROI raster scanning, which resulted in an approach time of less than 3 minutes. As the micropipette tip came into contact with the cell the resistance measured through the electrode increased from 2.7 M $\Omega$  to ~2.8 M $\Omega$ , triggering the system to stop. Shown in Fig. 5(a) is a representative DIC image of the final positioning of the micropipette. Similar to the fluorescent beads, the overall collected signal increased non-linearly as the labeled cells were approached, as shown in Fig. 5(b). Figure 5(c) shows an overlaid brightfield (DIC) and fluorescent (DAPI Filter Set) image and the spatial coordinates corresponding to peak signal acquisition per ROI scan.

#### 4. Discussion

In this work, real-time automated navigation of a micropipette was performed using two-way fluorescence feedback. In order to accomplish this, excitation light was guided to the tip of the electrode through an integrated tapered optical fiber. As shown in Fig. 1(b), the beam profile takes a cone-like shape, where the fluorescent intensity is brightest at the tip and decreases with distance. This beam profile enables changes in fluorescent signal based on the proximity between the intra-electrode tapered optical fiber and the sample. To maximize the fluence of the beam on the sample, the fiber tip and electrode aperture are proximally aligned to have a distance between 1-4  $\mu\text{m}$ . This distance enables high collection efficiency and allows a measurable increase in pipette resistance when the tip contacts the cell membrane. Resistances higher than 1.3 M $\Omega$  result in micropipette tapers that are too shallow for optimal fiber tip placement. This results in placement too far into the micropipette lumen, consequentially hindering fluorescence collection efficiency. Resistances lower than 1 M $\Omega$  allow the tip of the tapered fiber to go beyond the tip of the micropipette. This negatively affects resistance changes caused by close proximity between the electrode aperture and cell. Applications *in vivo* will require smaller tip diameters and larger resistances than those used *in-vitro*. *In-vivo* patch clamping work is often performed with higher resistances (e.g. 5-8 MOhms). While not tested in this study, resistances beyond the upper and lower range used are likely possible by changing the micropipette or tapered optical fiber architecture.

In order to properly position the micropipette tip on a labeled cell, it is important to have sufficient spatial resolution and detection sensitivity. A ~2.9  $\mu\text{m}$  FWHM, as shown in Fig. 2, using the intra-electrode tapered optical fiber reveals a measurement that is smaller than the nucleus, and therefore the soma, of the B35 neuroblastoma cells. This indicates that the resolution of the system should be adequate for positioning the electrode aperture on a targeted neuron. Sufficient detection sensitivity is demonstrated by scanning fluorescently labeled neurons, as shown in Fig. 3. However, substantial auto-fluorescence was generated in the tapered optical fiber by the 405 nm laser. The spectrum of the noise was measured using a spectrometer, after removing the emission filters from the optical path. The auto-fluorescence generated from the optical fiber was measured to have a Gaussian distribution with a peak signal at 545 nm with a FWHM of 153 nm. To minimize the noise reaching the detector, filters and spatial filtering were utilized. The camera in the system was used to visualize the spatial distribution of the auto-fluorescence, which is mainly generated from the cladding of the optical fiber. A pinhole was utilized to block auto-fluorescence from the cladding, while allowing light propagating out of the core to reach the detector. Improved sensitivity may be achievable through the use of different laser lines and fluorophores.

An automated approach algorithm was developed to determine whether fluorescence intensity could be used as feedback to determine proximity between the micropipette tip and the sample. The algorithm starts by raster scanning a large ROI in the 2D x-y plane and subsequently descending along the z direction. After signal detection occurs, a small ROI scan is performed.

At sufficiently close distances there is a relatively large increase in the fluorescence signal, as shown in Fig. 4(c). For these situations, a simple photon count threshold can determine signal detection. At larger distances between the intra-electrode tapered optical fiber and the sample, the increase in overall photon counts can be subtle. Here, signal detection can more readily be determined by including photon counts neighboring the peak signal, as opposed to a single spatial location. This is done by utilizing image processing-based object counting (see methods). A signal is determined by object counts below or equal to a threshold of 4. These results indicate that signal intensity threshold provides a sufficient method for approaching a target. Since large ROI scans took longer to complete than the small ROI scans, the overall approach time (< 8 minutes for cells) was highly dependent on switching between scan sizes quickly. Prolonged approach times result in photobleaching of the cell, visible in real-time on the microscope camera as well as within the photon count rate. This method of determining signal detection resulted in successful automated approach to fluorescent beads and labeled neurons, as shown in Figs. 4 and 5. Future studies will investigate the formation of a giga-seal using the system. These results indicate that the fluorescence intensity can be used as feedback to determine proximity between the micropipette tip and the sample, allowing for an automated approach.

## 5. Conclusion

We present a novel method for performing fluorescence guided automated neuronal approach capable of robotically positioning the micropipette electrode tip directly upon neurons *in vitro*. The system presented here is, to the best of our knowledge, the first to develop an intra-electrode tapered optical fiber for automated neuronal approach utilizing fluorescence feedback. The use of a tapered fiber to both provide excitation light and capture emitted fluorescence at the micropipette tip couples the feedback mechanism directly to the distance between the target and electrode aperture, while also allowing for the detection of cell-specific labels. This is performed independent of traditional microscope-based imaging approaches. The use of fluorescence is ubiquitous in neuroscience where fluorescent tags are often used to label specific neuronal subtypes [28–30] or measure membrane potentials with ion [31–34] or voltage indicators [35–38]. Future work will investigate the use of intra-electrode tapered optical fibers in animal studies *in-vivo* to target fluorescently labeled neurons for photometry [24,39–41], optogenetics [42–45], and patch clamping. Although our data shows that the system can identify and approach specific cells of interest, further work is necessary to determine the ability of the system to target cells within the same local circuit. Technologies that enable neuronal targeting beyond that of the working distance of microscope objectives will provide valuable insights into cellular activity in the deep brain.

**Funding.** Division of Chemical, Bioengineering, Environmental, and Transport Systems (1944846); Flinn Foundation (FP21738).

**Acknowledgments.** We would like to acknowledge Douglas Daniel from the Ultrafast Laser Facility, part of the Chemical and Environmental Characterization Core Facilities at Arizona State University for his research support.

**Disclosures.** The authors declare no conflicts of interest.

**Data availability.** Data underlying the results presented in this paper are not publicly available at this time but may be obtained from the authors upon reasonable request.

## References

1. B. Sakmann and E. Neher, "Patch clamp techniques for studying ionic channels in excitable membranes," *Annu. Rev. Physiol.* **46**(1), 455–472 (1984).
2. M. Véléz-Fort, C. V. Rousseau, C. J. Niedworok, I. R. Wickersham, E. A. Rancz, A. P. Brown, M. Strom, and T. W. Margrie, "The stimulus selectivity and connectivity of layer six principal cells reveals cortical microcircuits underlying visual processing," *Neuron* **83**(6), 1431–1443 (2014).
3. S. B. Kodandaramaiah, G. T. Franzesi, B. Y. Chow, E. S. Boyden, and C. R. Forest, "Automated whole-cell patch-clamp electrophysiology of neurons *in vivo*," *Nat. Methods* **9**(6), 585–587 (2012).

4. G. L. Holst, W. Stoy, B. Yang, I. Kolb, S. B. Kodandaramaiah, L. Li, U. Knoblich, H. Zeng, B. Haider, E. S. Boyden, and C. R. Forest, "Autonomous patch-clamp robot for functional characterization of neurons in vivo: development and application to mouse visual cortex," *J. Neurophysiol.* **121**(6), 2341–2357 (2019).
5. H.-J. Suk, I. van Welie, S. B. Kodandaramaiah, B. Allen, C. R. Forest, and E. S. Boyden, "Closed-loop real-time imaging enables fully automated cell-targeted patch-clamp neural recording in vivo," *Neuron* **95**(5), 1037–1047.e11 (2017).
6. L. A. Annecchino, A. R. Morris, C. S. Copeland, O. E. Agabi, P. Chadderton, and S. R. Schultz, "Robotic automation of in vivo two-photon targeted whole-cell patch-clamp electrophysiology," *Neuron* **95**(5), 1048–1055.e3 (2017).
7. I. Kolb, W. Stoy, E. Rousseau, O. Moody, A. Jenkins, and C. Forest, "Cleaning patch-clamp pipettes for immediate reuse," *Sci. Rep.* **6**(1), 35001 (2016).
8. S. B. Kodandaramaiah, F. J. Flores, G. L. Holst, A. C. Singer, X. Han, E. N. Brown, E. S. Boyden, and C. R. Forest, "Multi-neuron intracellular recording in vivo via interacting autpatching robots," *eLife* **7**, e24656 (2018).
9. N. S. Desai, J. J. Siegel, R. A. Chitwood, and D. Johnston, "Matlab-based automated patch-clamp system for awake behaving mice," *J. Neurophysiol.* **114**(2), 1331–1345 (2015).
10. D. Vasilyev, T. Merrill, A. Iwanow, J. Dunlop, and M. Bowlby, "A novel method for patch-clamp automation," *Pfluegers Arch.* **452**(2), 240–247 (2006).
11. B. Long, L. Li, U. Knoblich, H. Zeng, and H. Peng, "3d image-guided automatic pipette positioning for single cell experiments in vivo," *Sci. Rep.* **5**(1), 18426 (2015).
12. Q. Wu, I. Kolb, B. M. Callahan, Z. Su, W. Stoy, S. B. Kodandaramaiah, R. Neve, H. Zeng, E. S. Boyden, C. R. Forest, and A. A. Chubykin, "Integration of autpatching with automated pipette and cell detection in vitro," *J. Neurophysiol.* **116**(4), 1564–1578 (2016).
13. P. Novak, J. Gorelik, U. Vivekananda, A. I. Shevchuk, Y. S. Ermolyuk, R. J. Bailey, A. J. Bushby, G. W. Moss, D. A. Rusakov, D. Klenerman, D. M. Kullmann, K. E. Volynski, and Y. E. Korchev, "Nanoscale-targeted patch-clamp recordings of functional presynaptic ion channels," *Neuron* **79**(6), 1067–1077 (2013).
14. H.-J. Suk, E. S. Boyden, and I. van Welie, "Advances in the automation of whole-cell patch clamp technology," *J. Neurosci. Methods* **326**, 108357 (2019).
15. A. Hayar, C. Gu, and E. D. Al-Chaer, "An improved method for patch clamp recording and calcium imaging of neurons in the intact dorsal root ganglion in rats," *J. Neurosci. Methods* **173**(1), 74–82 (2008).
16. K. Kitamura, B. Judkewitz, M. Kano, W. Denk, and M. Häusser, "Targeted patch-clamp recordings and single-cell electroporation of unlabeled neurons in vivo," *Nat. Methods* **5**(1), 61–67 (2008).
17. B. K. Andrásfalvy, G. L. Galíñanes, D. Huber, M. Barbic, J. J. Macklin, K. Susumu, J. B. Delehanty, A. L. Huston, J. K. Makara, and I. L. Medintz, "Quantum dot-based multiphoton fluorescent pipettes for targeted neuronal electrophysiology," *Nat. Methods* **11**(12), 1237–1241 (2014).
18. S. Turtaev, I. T. Leite, T. Altwegg-Boussac, J. M. Pákan, N. L. Rochefort, and T. Čížmár, "High-fidelity multimode fibre-based endoscopy for deep brain in vivo imaging," *Light: Sci. Appl.* **7**(1), 92 (2018).
19. F. Pisanello, L. Sileo, I. A. Oldenburg, M. Pisanello, L. Martiradonna, J. A. Assad, B. L. Sabatini, and M. De Vittorio, "Multipoint-emitting optical fibers for spatially addressable in vivo optogenetics," *Neuron* **82**(6), 1245–1254 (2014).
20. M. Bianco, A. Balena, M. Pisanello, F. Pisano, L. Sileo, B. Spagnolo, C. Montinaro, B. L. Sabatini, M. De Vittorio, and F. Pisanello, "Comparative study of autofluorescence in flat and tapered optical fibers towards application in depth-resolved fluorescence lifetime photometry in brain tissue," *Biomed. Opt. Express* **12**(2), 993–1010 (2021).
21. D. Miyamoto and M. Murayama, "The fiber-optic imaging and manipulation of neural activity during animal behavior," *Neurosci. Res.* **103**, 1–9 (2016).
22. Y. Katz, O. Yizhar, J. Staiger, and I. Lampl, "Optopatcher—an electrode holder for simultaneous intracellular patch-clamp recording and optical manipulation," *J. Neurosci. Methods* **214**(1), 113–117 (2013).
23. D. L. Hunt, C. Lai, R. D. Smith, A. K. Lee, T. D. Harris, and M. Barbic, "Multimodal in vivo brain electrophysiology with integrated glass microelectrodes," *Nat. Biomed. Eng.* **3**(9), 741–753 (2019).
24. Y. Hirai, E. Nishino, and H. Ohmori, "Simultaneous recording of fluorescence and electrical signals by photometric patch electrode in deep brain regions in vivo," *J. Neurophysiol.* **113**(10), 3930–3942 (2015).
25. Y. LeChasseur, S. Dufour, G. Lavertu, C. Bories, M. Deschênes, R. Vallée, and Y. De Koninck, "A microprobe for parallel optical and electrical recordings from single neurons in vivo," *Nat. Methods* **8**(4), 319–325 (2011).
26. S. Dufour, G. Lavertu, S. Dufour-Beauséjour, A. Juneau-Fecteau, N. Calakos, M. Deschênes, R. Vallée, and Y. De Koninck, "A multimodal micro-optrode combining field and single unit recording, multispectral detection and photolabeling capabilities," *PLoS One* **8**(2), e57703 (2013).
27. C. Miranda, S. Sampath Kumar, J. Muthuswamy, and B. S. Smith, "Photoacoustic micropipette," *Appl. Phys. Lett.* **113**(26), 264103 (2018).
28. N. Tamamaki, Y. Yanagawa, R. Tomioka, J.-I. Miyazaki, K. Obata, and T. Kaneko, "Green fluorescent protein expression and colocalization with calretinin, parvalbumin, and somatostatin in the gad67-gfp knock-in mouse," *J. Comp. Neurol.* **467**(1), 60–79 (2003).
29. U. Knoblich, L. Huang, H. Zeng, and L. Li, "Neuronal cell-subtype specificity of neural synchronization in mouse primary visual cortex," *Nat. Commun.* **10**(1), 2533 (2019).
30. T.-W. Chen, T. J. Wardill, Y. Sun, S. R. Pulver, S. L. Renninger, A. Baohan, E. R. Schreiter, R. A. Kerr, M. B. Orger, V. Jayaraman, L. L. Looger, K. Svoboda, and D. S. Kim, "Ultrasensitive fluorescent proteins for imaging neuronal activity," *Nature* **499**(7458), 295–300 (2013).

31. Y. Qian, K. D. Piatkevich, B. Mc Larney, A. S. Abdelfattah, S. Mehta, M. H. Murdock, S. Gottschalk, R. S. Molina, W. Zhang, Y. Chen, J. Wu, M. Drobizhev, T. E. Hughes, J. Zhang, E. R. Schreiter, S. Shoham, D. Razansky, E. S. Boyden, and R. E. Campbell, "A genetically encoded near-infrared fluorescent calcium ion indicator," *Nat. Methods* **16**(2), 171–174 (2019).
32. M. Mank, A. F. Santos, S. Drenberger, T. D. Mrsic-Flogel, S. B. Hofer, V. Stein, T. Hendel, D. F. Reiff, C. Levelt, A. Borst, T. Bonhoeffer, M. Hübner, and O. Griesbeck, "A genetically encoded calcium indicator for chronic in vivo two-photon imaging," *Nat. Methods* **5**(9), 805–811 (2008).
33. M. Mank and O. Griesbeck, "Genetically encoded calcium indicators," *Chem. Rev.* **108**(5), 1550–1564 (2008).
34. M. Z. Lin and M. J. Schnitzer, "Genetically encoded indicators of neuronal activity," *Nat. Neurosci.* **19**(9), 1142–1153 (2016).
35. K. D. Piatkevich, E. E. Jung, C. Straub, C. Linghu, D. Park, H.-J. Suk, D. R. Hochbaum, D. Goodwin, E. Pnevmatikakis, N. Pak, T. Kawashima, C.-T. Yang, J. L. Rhoades, O. Shemesh, S. Asano, Y.-G. Yoon, L. Freifeld, J. L. Saulnier, C. Riegler, F. Engert, T. Hughes, M. Drobizhev, B. Szabo, M. B. Ahrens, S. W. Flavell, B. L. Sabatini, and E. S. Boyden, "A robotic multidimensional directed evolution approach applied to fluorescent voltage reporters," *Nat. Chem. Biol.* **14**(4), 352–360 (2018).
36. D. R. Hochbaum, Y. Zhao, S. L. Farhi, N. Klapoetke, C. A. Werley, V. Kapoor, P. Zou, J. M. Kralj, D. Maclaurin, N. Smedemark-Margulies, J. L. Saulnier, G. L. Boulting, C. Straub, Y. K. Cho, M. Melkonian, G. K.-S. Wong, D. J. Harrison, V. N. Murthy, B. L. Sabatini, E. S. Boyden, R. E. Campbell, and A. E. Cohen, "All-optical electrophysiology in mammalian neurons using engineered microbial rhodopsins," *Nat. Methods* **11**(8), 825–833 (2014).
37. Y. Gong, C. Huang, J. Z. Li, B. F. Grewe, Y. Zhang, S. Eismann, and M. J. Schnitzer, "High-speed recording of neural spikes in awake mice and flies with a fluorescent voltage sensor," *Science* **350**(6266), 1361–1366 (2015).
38. Y. Gong, M. J. Wagner, J. Z. Li, and M. J. Schnitzer, "Imaging neural spiking in brain tissue using fret-opsin protein voltage sensors," *Nat. Commun.* **5**(1), 3674 (2014).
39. A. A. Patel, N. McAlinden, K. Mathieson, and S. Sakata, "Simultaneous electrophysiology and fiber photometry in freely behaving mice," *Front. Neurosci.* **14**, 148 (2020).
40. F. Pisano, M. Pisanello, S. J. Lee, J. Lee, E. Maglie, A. Balena, L. Sileo, B. Spagnolo, M. Bianco, M. Hyun, M. D. Vittorio, B. L. Sabatini, and F. Pisanello, "Depth-resolved fiber photometry with a single tapered optical fiber implant," *Nat. Methods* **16**(11), 1185–1192 (2019).
41. Y. Sych, M. Chernysheva, L. T. Sumanovski, and F. Helmchen, "High-density multi-fiber photometry for studying large-scale brain circuit dynamics," *Nat. Methods* **16**(6), 553–560 (2019).
42. Y. Katz, M. Sokoletsky, and I. Lampl, "In-vivo optogenetics and pharmacology in deep intracellular recordings," *J. Neurosci. Methods* **325**, 108324 (2019).
43. W. Muñoz, R. Tremblay, and B. Rudy, "Channelrhodopsin-assisted patching: in vivo recording of genetically and morphologically identified neurons throughout the brain," *Cell Rep.* **9**(6), 2304–2316 (2014).
44. F. Pisanello, G. Mandelbaum, M. Pisanello, I. A. Oldenburg, L. Sileo, J. E. Markowitz, R. E. Peterson, A. D. Patria, T. M. Haynes, M. S. Emara, B. Spagnolo, S. R. Datta, M. D. Vittorio, and B. L. Sabatini, "Dynamic illumination of spatially restricted or large brain volumes via a single tapered optical fiber," *Nat. Neurosci.* **20**(8), 1180–1188 (2017).
45. M. Pisanello, F. Pisano, L. Sileo, E. Maglie, E. Bellistri, B. Spagnolo, G. Mandelbaum, B. L. Sabatini, M. De Vittorio, and F. Pisanello, "Tailoring light delivery for optogenetics by modal demultiplexing in tapered optical fibers," *Sci. Rep.* **8**(1), 4467 (2018).